Article ID: 1006-8775(2024)03-0230-11

Influences of Earth Incidence Angle on FY-3/MWRI SST Retrieval and Evaluation of Reprocessed SST

ZHANG Miao (张 淼)[1,2], CHEN Lin (陈 林)[1,2], XU Na (徐 娜)[1,2], CAO Guang-zhen (曹广真)[1,2]

(1. Key Laboratory of Radiometric Calibration and Validation for Environmental Satellites, National Satellite Meteorological Center, China Meteorological Administration, Beijing 100081 China; 2. Innovation Center for FengYun Meteorological Satellite (FYSIC), Beijing 100081 China)

Abstract: Sea surface temperature (SST) is a crucial physical parameter in meteorology and oceanography. This study demonstrates that the influence of earth incidence angle (EIA) on the SST retrieved from the microwave radiation imager (MWRI) onboard FengYun-3 (FY-3) meteorological satellites should not be ignored. Compared with algorithms that do not consider the influence of EIA in the regression, those that integrate the EIA into the regression can enhance the accuracy of SST retrievals. Subsequently, based on the recalibrated Level 1B data from the FY-3/MWRI, a long-term SST dataset was reprocessed by employing the algorithm that integrates the EIA into the regression. The reprocessed SST data, including FY-3B/MWRI SST during 2010–2019, FY-3C/MWRI SST during 2013–2019, and FY-3D/MWRI SST during 2018–2020, were compared with the in-situ SST and the SST dataset from the Operational Sea Surface Temperature and Ice Analysis (OSTIA). The results show that the FY-3/MWRI SST data were consistent with both the in-situ SST and the OSTIA SST dataset. Compared with the Copernicus Climate Change Service V2.0 SST, the absolute deviation of the reprocessed SST, with a quality flag of 50, was less than 1.5°C. The root mean square errors of the FY-3/MWRI orbital, daily, and monthly SSTs, with a quality flag of 50, were approximately 0.82°C, 0.69°C, and 0.37°C, respectively. The primary discrepancies between the FY-3/MWRI SST and the OSTIA SST were found mainly in the regions of the western boundary current and the Antarctic Circumpolar Current. Overall, this reprocessed SST product is recommended for El Niño and La Niña events monitoring.

Key words: FengYun-3 satellites; sea surface temperature; microwave radiation imager; earth incidence angle; reprocessing

CLC number: P405 **Document code:** A

Citation: ZHANG Miao, CHEN Lin, XU Na, et al. Influences of Earth Incidence Angle on FY-3/MWRI SST Retrieval and Evaluation of Reprocessed SST [J]. Journal of Tropical Meteorology, 2024, 30(3): 230–240, https://doi.org/10.3724/j.1006-8775.2024.021

1 INTRODUCTION

Sea surface temperature (SST) serves as a vital physical parameter in meteorology and oceanography (Qian et al. [1]; Chen et al. [2]; Guo et al. [3]; Pisano et al. [4]), influencing aspects such as ocean circulation, atmospheric circulation, and marine weather and climate (Liu et al. [5]; Dong et al. [6]; Bi and Li [7]; Bulgin et al. [8]). In the early stage, SST measurements primarily relied on ships and buoys (Kennedy [9]; Banzon et al. [10]), but such measurements cannot meet the demands of large-scale real-time monitoring (Pastor et al. [11]). Satellite remote sensing technology, with its advantages of wide coverage, high resolution, and long-term repeatable observation, has been widely applied in global SST monitoring (Gentemann et al. [12]; Zhang et al. [13]). SST monitoring through satellites predominantly employs both infrared remote sensing and passive microwave remote sensing techniques (Ricciardulli and Wentz [14]). Although infrared remote sensing has a high resolution, it is hindered by cloud cover, and the retrieval accuracy is susceptible to the diurnal variations in solar radiation, water vapor, and aerosols (Wentz et al. [15]). In contrast, although microwave remote sensing features lower resolution and is susceptible to sea surface roughness, it can effectively overcome the limitations of infrared remote sensing, enabling all-weather observations (Wentz et al. [16]).

The development of spaceborne microwave radiometers in China started relatively late, and FengYun-3 (FY-3) satellites are the second-generation polar-orbiting meteorological satellites of China (Zhang et al. [17]). Since the launch of the FY-3A satellite in 2008, a total of seven satellites (FY-3A/3B/3C/3D/3E/3F/3G) have been successfully launched, among which FY-3A, FY-3B, FY-3C, FY-3D, FY-3F, and FY-3G satellites carry microwave radiation imagers (MWRI) (Xia et al. [18]). The MWRI scans conically at an earth incidence angle (EIA) of 53.0° with a variation range of approximately 0.8°. Yang et al. found that in the ocean, a 2° variation range of the EIA could result in a brightness temperature difference of 6 K

Received 2024-02-19; **Revised** 2024-05-15; **Accepted** 2024-08-15

Funding: National Natural Science Foundation of China (42330602); Youth Innovation Team for "FengYun Satellite Remote Sensing Product Verification" (CMA2023QN12)

Biography: ZHANG Miao, Senior Engineer, primarily undertaking research on satellite oceanography, and retrieval and fusion of sea surface temperature from FengYun satellite remote sensing.

Corresponding author: CHEN Lin, e-mail: chenlin@cma.gov.cn

at a lower-frequency (e.g. 10.65 GHz) vertical-polarization channel [19]. However, at a higher frequency and under land conditions, the impact of EIA on brightness temperature can be negligible (Yang et al. [19]; He et al. [20]). The algorithm theoretical basis document of the ocean algorithm for the Advanced Microwave Scanning Radiometer for the Earth Observing System indicates that achieving an SST retrieval accuracy of 0.5°C requires the known accuracy of EIA to be 0.05° (Wentz et al. [21]). The retrieval of the FY-3/MWRI SST employs statistical algorithms that are based on the statistical relationship between buoy observations and microwave brightness temperature (Zhang et al. [22]; Zhang et al. [23]). The 10.65 GHz channel serves as the most crucial channel for SST retrievals, yet the regression algorithms do not account for the impacts of EIA.

In this research, we examined the influences of EIA on SST retrievals. Moreover, based on the recalibrated FY-3/MWRI Level 1B data (He et al. [20]; Yao et al. [24]), a regression algorithm that incorporates EIA in the retrieval was established and then applied to reprocess the SST datasets, aiming to derive a high-precision long-term SST dataset. Furthermore, a statistical evaluation of the reprocessed FY-3/MWRI SST was conducted. The remainder of this paper is organized as follows.

The data and methods are provided in Section 2. Section 3 analyzes the influences of EIA on SST retrievals. The statistical evaluation of the reprocessed FY-3/MWRI SST is presented in Section 4. Finally, Section 5 presents the conclusions.

2 DATA AND METHODS

2.1 *Data*

In-situ SST and global analysis SST are two types of reference SST data commonly used for quality validation of SST products (Xu and Ignatov [25]; Wang et al. [26]; Zhao et al. [27]; Huang et al. [28]).

In the present study, the in-situ SST data used to calculate regression coefficients and verify SST products were obtained from the in-situ SST Quality Monitor System (Zhang et al. [29]). This system is maintained by the Center for Satellite Applications and Research, National Oceanic and Atmospheric Administration/National Environmental Satellite, Data and Information Service. It ensures strict quality control for in-situ data and assigns quality flags to Global Telecommunication System SST (Petrenko et al. [30]). The in-situ data are available online at https://www.star.nesdis.noaa.gov/socd/sst/iquam/data.html/. In this study, only drifting and mooring buoy SST data with the highest quality flag of 5 were utilized.

The Operational SST and Sea Ice Analysis (OSTIA) SST dataset was developed by the UK Met Office using the multi-scale optimal interpolation technology to fuse the in-situ SST data with the SST data from the Advanced Very-High-Resolution Radiometer, Advanced Microwave Scanning Radiometer, Tropical Rainfall Measuring Mission Microwave Imager, Advanced Along-Track Scanning Radiometer and Spinning Enhanced Visible and Infrared Imager. The OSTIA system can provide near real-time daily SST data at a resolution of 5 km and monthly SST data at a resolution of 25 km, and the errors of these data are less than 0.3°C (Good et al. [31]). The OSTIA SST data are available online at https://data.marine.copernicus.eu/product/SST_GLO_SST_L4_NRT_OBSERVATIONS_010_001/. In this study, the OSTIA SST data were utilized to evaluate the accuracy of the FY-3/MWRI SST data. Due to the coarse spatial resolution (25 km) of the daily MWRI SST, the daily OSTIA SST within the MWRI grid was averaged and compared with the daily MWRI SST.

2.2 *Methods*

The SST retrieval primarily relies on the 10.7 GHz channel. Given that the atmospheric interference is quite small at 10.65 GHz and that the effects of wind and atmospheric conditions can be removed by using different channel combinations, eight channels of the FY-3/MWRI at 10.65 GHz, 18.7 GHz, 23.8 GHz, and 36.5 GHz, each with dual polarization, were used for SST retrieval. Firstly, MWRI precipitation and sea-ice products (available online at http://satellite.cma.gov.cn/portalsite/default.aspx) were utilized to eliminate pixels with precipitation and sea ice. Subsequently, descending and ascending regression coefficients were derived through regression calculation based on the matched data of satellite-based brightness temperature and quality-controlled in-situ SST data. For reprocessing, the regression coefficients were obtained by using the matched data for 15 days before and after the retrieval day, while for operational applications, the matched data for the closest 30 days before the retrieval day were utilized. The retrieval method is presented in Eq. 1:

$$T_s = a_0 + \sum_{i=1}^{8}\left(a_i t_i + b_i t_i^2\right) \tag{1}$$

where T_s denotes the retrieved SST. For the observed brightness temperature at 10.65 GHz, 18.7 GHz and 36.5 GHz, $t_i = T_{Bi} - 150$. For the observed brightness temperature at 23.8 GHz, $t_i = -\ln(290 - T_{Bi})$, where T_B represents the brightness temperature observed from the MWRI at the corresponding frequency and polarization. Variables a and b represent regression coefficients. The retrieval method was detailed in Zhang et al. [22]. Pixels were categorized into three groups with quality flags of 50 (high quality), 51 (medium quality), and 52 (poor quality), and compared with the Copernicus Climate Change Service (C3S) V2.0 SST (Merchant [32]). The absolute deviations of the SST in these three types of pixels were less than 1.5°C, between 1.5°C and 2.5°C, and more than 2.5°C, respectively.

The SST data with a quality flag of 52 contained information such as positioning anomalies, calibration anomalies, undetected precipitation and sea ice, land interference, high wind speed, and extreme weather. It is beneficial for analyzing the fundamental causes of errors and improving product quality as users can choose the SST

data with different quality flags according to their needs.

For the synthesis of daily data, to avoid the impact of poor-quality SST data, the number of pixels with quality flags of 50, 51, and 52 within the grid was calculated. If the maximum count corresponded to pixels with a quality flag of 50, the SSTs on those pixels were averaged, and the grid quality flag was assigned 50. If the maximum number count corresponded to pixels with a quality flag of 51, the SSTs on the pixels with quality flags of 50 and 51 were averaged, and the grid quality flag was assigned 51. If the maximum count corresponded to pixels with the quality flag of 52, the SSTs on all pixels were averaged, and the grid quality flag was assigned 52. For the synthesis of monthly and annual data, regions impacted by sea ice were flagged, i.e., only complete years were considered for the average estimate in each grid point (Yang et al. [33]).

3 INFLUENCE OF EARTH INCIDENCE ANGLE ON SST RETRIEVALS

3.1 *Sensitivity analysis of channel brightness temperature to earth incidence angle*

The microwave radiation observed by satellites predominantly includes surface radiation after atmospheric attenuation, atmospheric microwave radiation reflected by the surface and returned to space, and atmospheric microwave radiation directed to space. The radiative transfer equation for satellite microwave remote sensing is presented in Eq. 2:

$$T_{B\lambda}^{\uparrow}(\infty)=\alpha_{S\lambda}T_S\mathrm{e}^{-\int_0^{\infty}\alpha_{\lambda}\mathrm{d}l}+\int_0^{\infty}T(l)\left[(1-\alpha_{S\lambda})\mathrm{e}^{-2\int_0^{l}\alpha_{\lambda}\mathrm{d}l'}+1\right]\mathrm{e}^{-\int_l^{\infty}\alpha_{\lambda}\mathrm{d}l'}\alpha_{\lambda}\mathrm{d}l \quad (2)$$

where $T_{B\lambda}^{\uparrow}(\infty)$ denotes the microwave radiation observed by satellites, $\alpha_{S\lambda}$ denotes surface emissivity, T_S denotes surface temperature, α_{λ} is a function of atmospheric absorption medium density, T denotes atmospheric temperature, and l denotes the transmission path. The emissivity of the ocean surface between 6 GHz and 90 GHz depends on various parameters such as frequency, polarization, EIA, wind speed, wind direction, and SST by means of the Fresnel equations (Eq. 3) (Meissner and Wentz [34]). Consequently, through radiative transfer calculations, the sensitivity of channel brightness temperature to the EIA can be analyzed.

$$\alpha_{S\lambda}=1-|r_p|^2,\ p=v,\ h$$
$$r_v=\frac{\varepsilon\cos\theta-\sqrt{\varepsilon-\sin^2\theta}}{\varepsilon\cos\theta+\sqrt{\varepsilon-\sin^2\theta}} \quad (3)$$
$$r_h=\frac{\cos\theta-\sqrt{\varepsilon-\sin^2\theta}}{\cos\theta+\sqrt{\varepsilon-\sin^2\theta}}$$

where v denotes vertical polarization, h denotes horizontal polarization, ε denotes the complex dielectric constant of sea water, and θ denotes EIA.

The standard atmospheric profile and the EIA were inputted into the vector discrete-ordinate radiative transfer model (Weng [35]) to simulate the variation of brightness temperature with the EIA on a calm ocean surface at different frequencies and polarization channels, which were used to retrieve the MWRI SST. Fig. 1 illustrates the variation of brightness temperature with the EIA at different frequencies and polarizations. It is evident that for vertically polarized channels, the brightness temperature rose with the increase of the EIA, and the brightness temperature at a lower frequency varied greatly across different EIAs. Specifically, when the EIA changed by 1°, which was the variation range of FY-3 MWRI EIAs, the brightness temperature varied by approximately 3 K. Conversely, for horizontally polarized channels, the brightness temperature in channels 10H, 19H, and 37H

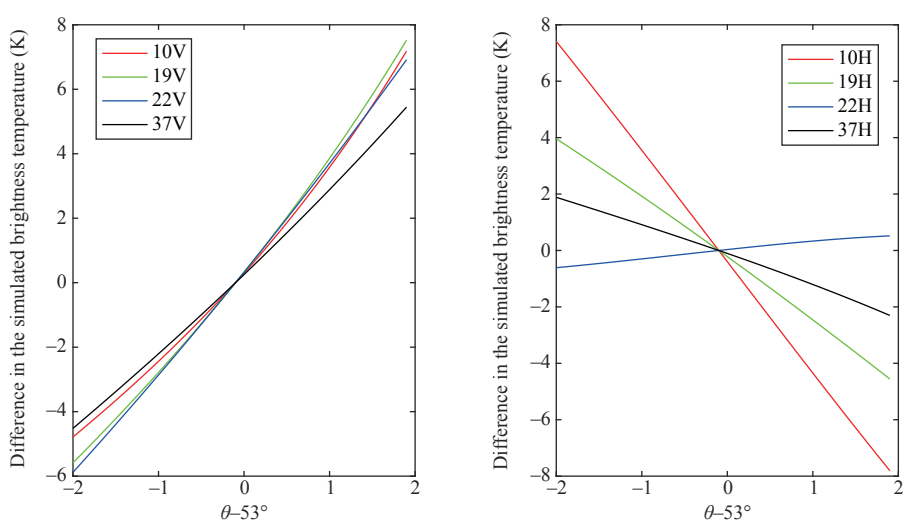


Figure 1. Variations of brightness temperature with earth incidence angle (EIA) at different frequencies and polarizations simulated by the vector discrete ordinate radiative transfer model. The horizontal axis represents the difference between the EIA (θ) and 53.0°, and the vertical axis signifies the difference between the simulated brightness temperature at different EIAs and the simulated brightness temperature at the 53.0° EIA. Different colors denote diverse frequencies and (a) vertical and (b) horizontal polarizations. For instance, 10V(H) corresponds to 10 GHz vertical (horizontal) polarization channels.

decreased with the increase of the EIA, whereas the brightness temperature in channel 22H rose with the EIA. This finding underscores the significance of considering the influence of EIA on microwave brightness temperature.

3.2 *Sensitivity analysis of SST biases to earth incidence angle*

At a 30-minute time matching and a 25-km spatial matching, the biases of the FY-3G MWRI SST at different EIAs (with an interval of 0.1°) in August 2023 relative to the matched in-situ SST data were analyzed (Fig. 2a). The absence of MWRI channels near 7 GHz, which were sensitive to relatively low SST, resulted in positive SST biases at high latitudes (Gentemann et al. [36]; Zhang et al. [22]). To remove the influence of positive biases at high latitudes, the deviations at different EIAs between 35°N and 35°S were also analyzed (Fig. 2b). It is evident that the biases between 35°N and 35°S were markedly reduced compared with all samples at larger EIAs, indicating that the influence of the positive SST biases at high latitudes was effectively excluded. However, both Fig. 2a and Fig. 2b illustrate that when the EIA was less than 53°, the SST bias was negative, and the magnitude of the negative bias increased as the EIA decreased. Conversely, when the EIA exceeded 53°, the bias became positive, and its magnitude increased with the EIA. This result indicates that the impact of the EIA on the SST bias should not be ignored.

3.3 *Retrieval algorithm integrating earth incidence angle in the regression*

From Fig. 1, we know that brightness temperature was approximately proportional to EIA. Moreover, if the influence of atmospheric and oceanic emissivity was not considered, SST was approximately proportional to 10.7 GHz channel brightness temperature (Li et al. [37]). Therefore, according to the method mentioned in Section 2, the EIA was integrated as an additional proportional term in the regression (Eq. 4). The retrieved SST was compared with that obtained from the retrieval algorithm without the EIA in the regression. Fig. 3 illustrates the distributions of EIA and the difference between the MWRI SST obtained based on the two algorithms and the OSTIA SST on September 25, 2023. The results indicate that when the algorithm that integrates the EIA in the regression was employed, the areas with larger biases were significantly reduced compared with the results from the algorithm without considering the EIA in the regression. Furthermore, the biases were closer to 0°C, and the dependence of these biases on the EIA was also noticeably diminished, although local areas may exhibit worse results than before.

$$T_s = a_0 + a_1\theta + \sum_{i=2}^{10}\left(a_i t_i + b_i {t_i}^2\right) \tag{4}$$

where θ represents EIA.

Table 1 presents the statistical results of the errors of the retrieved SST compared with the OSTIA SST in September 2023. It is evident that compared with the results from the algorithm without considering the EIA in the regression, the proportion of samples with a quality flag of 50 for the algorithm that considered the EIA in the regression increased by approximately 7%, and the root mean square error (RMSE) of the SST decreased by about 0.35°C.

The retrieval algorithm for the FY-3B/3C/3D MWRI SST did not consider the impact of the EIA. The statistical relationship was analyzed at four latitudes (Zhang et al. [22]) to eliminate the influence of the EIA to a certain extent (the EIA exhibits noticeable latitude characteristics, as shown in Figs. 3a and Fig. 3b). However, this segmentation resulted in discontinuity at the latitude boundaries. Therefore, based on the recalibrated Level 1B data from the FY-3/MWRI, a high-precision long-term SST dataset was reprocessed by using the algorithm incorporating the EIA in the regression.

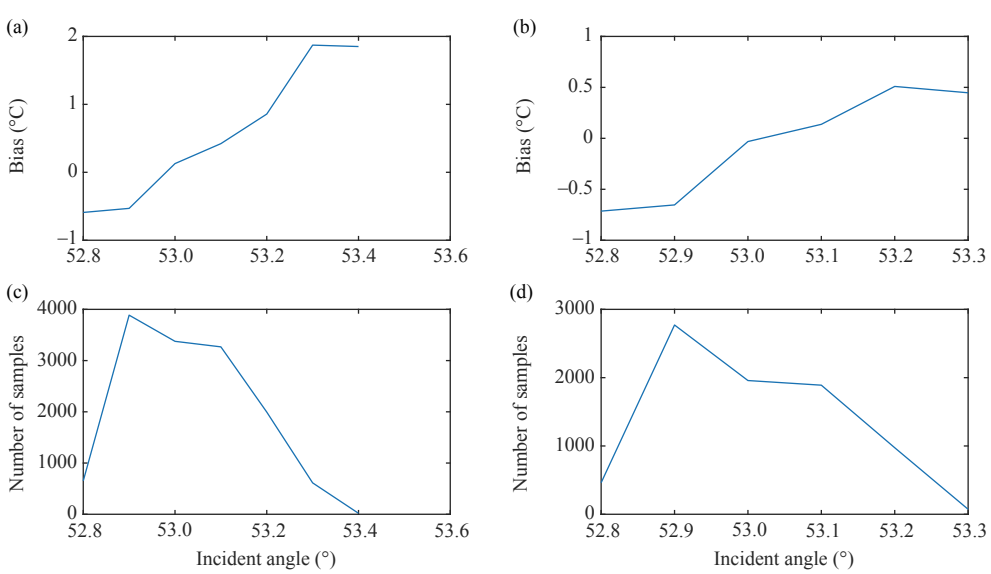


Figure 2. Variations of the sea surface temperature (SST) biases relative to the in-situ SST with the EIA for (a) all samples and (b) the samples between 35°N and 35°S, and (c) and (d) their corresponding number of samples.

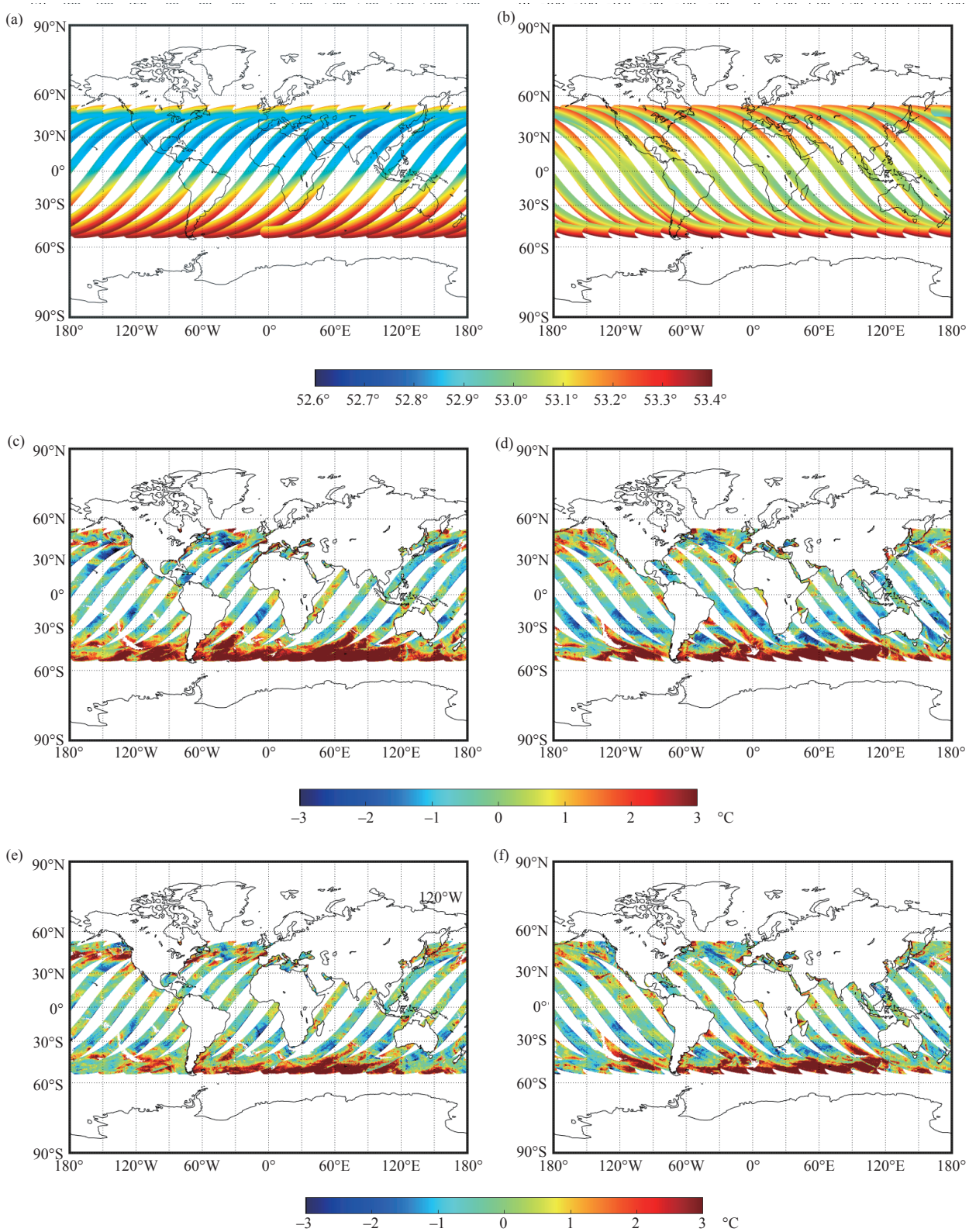


Figure 3. Distributions of (a, b) the EIA and the difference between the MWRI SST from the algorithms (e, f) with and (c, d) without the EIA in the regression relative to the OSTIA SST for (a, c, e) ascending orbit and (b, d, f) descending orbit on September 25, 2023.

4 STATISTICAL EVALUATION OF REPROCESSED FY-3/MWRI SST

The product types, time span, resolution, format, and coverage of the reprocessed FY-3/MWRI SST are presented in Table 2.

4.1 *Evaluation of the FY-3/MWRI orbital SST*

In this section, the reprocessed FY-3/MWRI orbital SST is evaluated by using the matched in-situ SST at a

Table 1. Statistical results of the errors of the retrieved SST relative to the OSTIA SST in September 2023.

Algorithm	Quality level	Sample proportion	Bias (°C)	RMSE (°C)
Algorithm without the EIA in the regression	Quality flag of 50	64%	−0.02	0.69
	Quality flag of 51	14%	0.47	1.72
	Quality flag of 52	22%	2.50	5.20
	All samples	100%	0.59	2.50
Algorithm with the EIA in the regression	Quality flag of 50	71%	0.02	0.66
	Quality flag of 51	13%	0.70	1.70
	Quality flag of 52	16%	2.21	4.90
	All samples	100%	0.46	2.15

Table 2. The product types, time span, resolution, format, and coverage of the reprocessed FY-3 MWRI SST.

Product type	Time span	Resolution	Format	Coverage
Orbital SST [45]	FY-3B: 2010/11/27–2019/08/04	51 km × 85 km	HDF	Global
Daily SST [46]	FY-3C: 2013/10/14–2019/12/16	0.25° × 0.25°		
Monthly SST [47]	FY-3D: 2018/01/16–2020/05/10			

30-minute time matching and 25-km spatial matching. Fig. 4 presents the time series of the global daily statistics of the FY-3B/3C/3D SST (with a quality flag of 50) relative to the in-situ SST. The results indicate that the biases of the FY-3 SST ranged from −0.2°C to 0.2°C, and the RMSEs of the FY-3 SST varied in the range of 0.7°C–0.9°C, both of which were generally stable. The statistical results in Table 3 indicate that the FY-3/MWRI SST with a quality flag of 50 had a RMSE of approximately 0.82°C, with a sample proportion exceeding 65% for this quality level. The MWRI measured the top millimeter of the ocean (Gentemann et al. [38]), whereas in-situ measurements were carried out at a depth of 1 m. During the daytime, increased solar insolation could lead to thermal stratification in the upper layer of the ocean under a low wind speed condition (Liu et al. [39]), resulting in the difference between the MWRI SST and the in-situ SST (Gentemann et al. [40]). Consequently, the error statistics of the daytime MWRI SST were higher than those for the nighttime. To reduce the effect of diurnal warming on the SST bias, SST measurements with corresponding wind speed less than 6 m s^{-1} and between 10:00 am and 06: 00 pm should be excluded in future statistics (Wentz et al. [17]).

4.2 *Evaluation of the daily FY-3/MWRI SST*

The reprocessed daily FY-3/MWRI SST was evaluated based on the daily OSTIA SST. Fig. 5 illustrates the time series of the global daily statistics of the FY-3B/3C/3D SST (with a quality flag of 50) relative to the OSTIA SST. The FY-3 SST biases ranged from −0.2°C to 0.2°C, and the RMSEs of the FY-3 SST varied in the range of 0.6°C–0.8°C, both demonstrating overall stability. The statistical results in Table 4 indicate that the FY-3/MWRI SST with a quality flag of 50 had an accuracy of approximately 0.69°C, with a sample proportion exceeding 70% for this quality level.

4.3 *Evaluation of the monthly FY-3/MWRI SST*

The reprocessed monthly FY-3/MWRI SST was

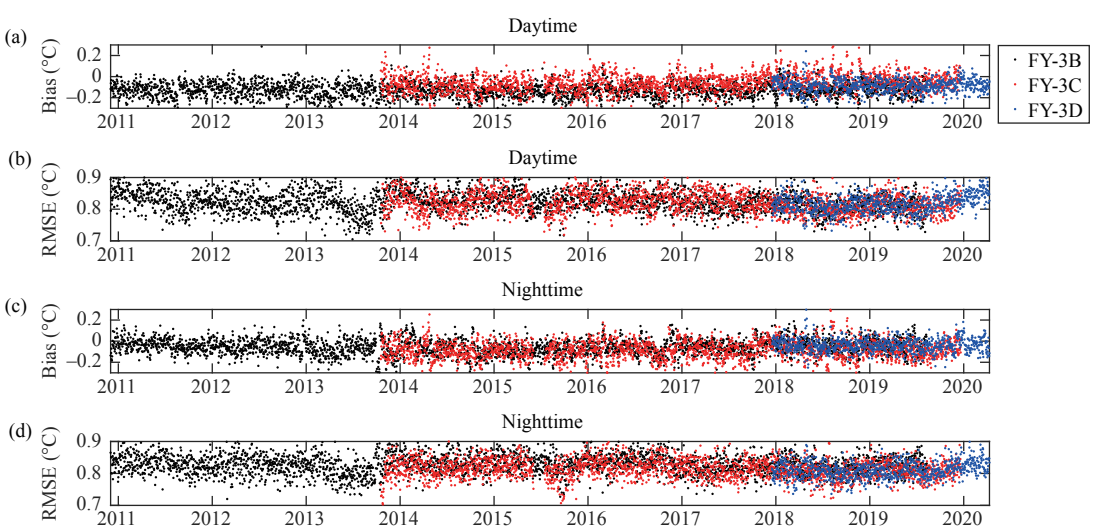


Figure 4. Time series of the (a, c) bias and (b, d) RMSE for FY-3B/3C/3D orbital SST with a quality flag of 50 relative to in-situ SST during the (a, b) daytime and (c, d) nighttime.

Table 3. Statistical comparison between FY-3 orbital SST and in-situ SST.

Period	Quality level	Sample proportion	Bias (°C)	RMSE (°C)
Daytime	Quality flag of 50	67.42%	−0.09	0.82
	Quality flag of 51	19.24%	0.12	1.92
	Quality flag of 52	13.44%	1.39	3.67
	All samples	100%	0.11	1.58
Nighttime	Quality flag of 50	71.36%	−0.06	0.82
	Quality flag of 51	18.49%	−0.03	1.91
	Quality flag of 52	10.15%	1.19	3.60
	All samples	100%	0.07	1.62

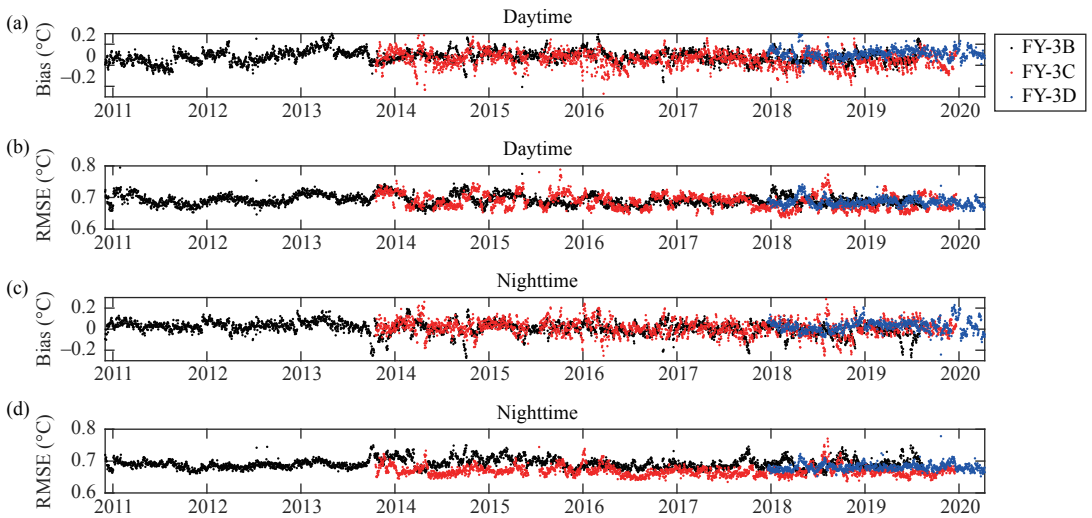


Figure 5. Same as Fig. 4, but for FY-3 daily SST compared with the daily OSTIA SST.

Table 4. Same as Table 3, but for FY-3 daily SST compared with the daily OSTIA SST.

Period	Quality level	Sample proportion	Bias (°C)	RMSE (°C)
Daytime	Quality flag of 50	70.17%	0.08	0.69
	Quality flag of 51	15.48%	0.73	1.86
	Quality flag of 52	14.35%	2.80	3.89
	All samples	100%	0.58	1.74
Nighttime	Quality flag of 50	74.48%	0.03	0.68
	Quality flag of 51	14.60%	0.43	1.86
	Quality flag of 52	10.92%	2.44	3.85
	All samples	100%	0.34	1.58

evaluated by comparing it with the monthly OSTIA SST. Fig. 6 shows the time series of the global monthly statistics of the FY-3B/3C/3D SST with a quality flag of 50 relative to the OSTIA SST. The biases of the FY-3 SST ranged from −0.2°C to 0.2°C, and the RMSEs of the FY-3 SST varied between 0.2°C and 0.6°C, both indicating overall stability. The statistics in Table 5 suggest that the accuracy of FY-3/MWRI SST with a quality flag of 50 was approximately 0.37°C, and the sample proportion was around 95% for this quality level. Spatial and temporal averaging effectively reduced random errors, and thus, the accuracy of the monthly SST was better than that of the daily SST.

Monthly FY-3 SST exhibited coherent variations across different latitudes compared with the OSTIA SST, as illustrated in Fig. 7. The temporal variability distinctly exhibited an annual oscillation, with the maximum amplitude observed in latitudes of 20°–50°N and the minimum amplitude in latitudes of 20°N–35°S.

4.4 *Intercomparisons of the annual mean SST*

Figure 8 displays the spatial distributions of the annual mean FY-3B/3C/3D SST and OSTIA SST from 2010 to 2020, as well as their difference. The spatial characteristics of the two datasets exhibited similar distribution patterns, i.e., higher SST in tropical regions, moderate SST at middle latitudes, and lower SST in polar regions. The primary differences between the FY-3/MWRI SST and the OSTIA SST were in the regions of the western boundary current and the Antarctic Circumpolar Current.

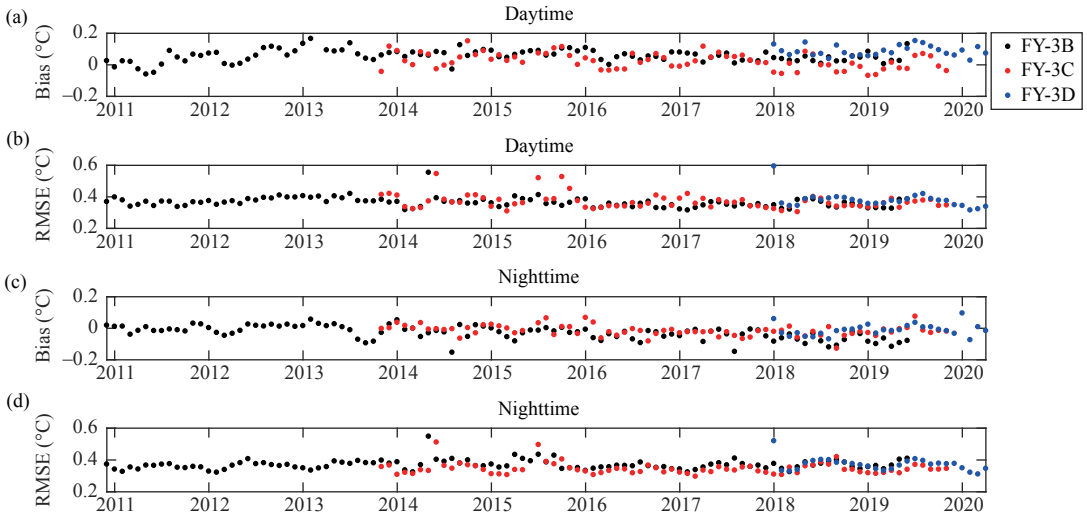


Figure 6. Same as Fig. 5, but for monthly SST.

Table 5. Same as Table 4, but for monthly SST.

Period	Quality level	Sample proportion	Bias (°C)	RMSE (°C)
Daytime	Quality flag of 50	94.38%	0.05	0.37
	Quality flag of 51	1.93%	0.58	1.32
	Quality flag of 52	3.69%	2.06	2.74
	All samples	100%	0.14	0.63
Nighttime	Quality flag of 50	96.44%	−0.02	0.36
	Quality flag of 51	1.67%	0.12	1.32
	Quality flag of 52	1.89%	1.79	2.93
	All samples	100%	0.02	0.54

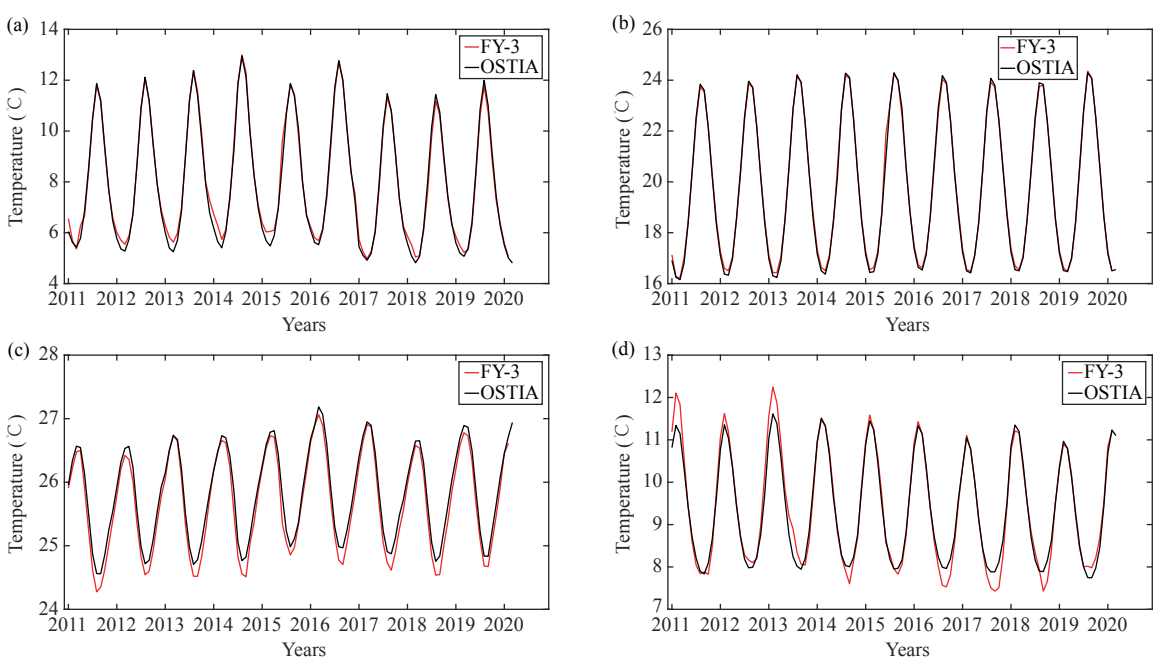


Figure 7. Time series of the monthly SST from 2011 to 2020 at latitudes of (a) 50°–90°N, (b) 20°–50°N, (c) 20°N–35°S, and (d) 35°–90°S.

4.5 *Niño-3.4 index*

SST has been widely used in climate studies, and the Niño-3.4 index is one of the most frequently utilized indexes for monitoring the occurrence and variability of El Niño and La Niña events. The Niño-3.4 index is defined as the average equatorial SST anomaly across the Pacific in

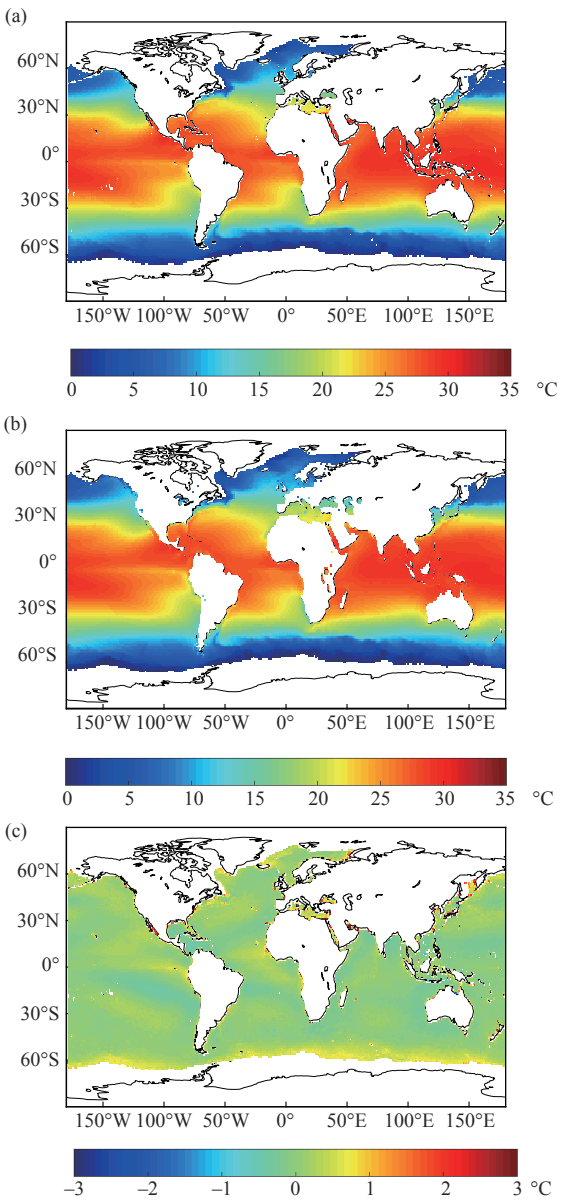


Figure 8. Spatial distributions of the annual mean (a) FY-3 SST and (b) OSTIA SST from 2010 to 2020, and (c) their difference.

the region of 5°N–5°S, 120°–170°W (Trenberth et al. [41]). Fig. 9 shows the temporal evolution of the Niño-3.4 index, calculated by subtracting the area-averaged FY-3 SST from the 30-year monthly mean optimum interpolation SST (from 1982 to 2011) (Reynolds et al. [42]), for the period from 2010 to 2020. In this research, all pixels of the FY-3 SST were included, as pixels with a quality flag of 50 may remove the anomalous SST. The temporal evolution of the Niño-3.4 SST anomaly exhibited remarkable similarity both for the reprocessed SST and the OSTIA SST, with only slight differences (Fig. 9). The strong El Niño events that occurred during 2015–2016 were faithfully reproduced with a comparable intensity by both the reprocessed SST and the OSTIA SST. However, there was a significant difference between the CMA operational SST (available at http://satellite.nsmc.org.cn/portalsite/default.aspx) and the OSTIA

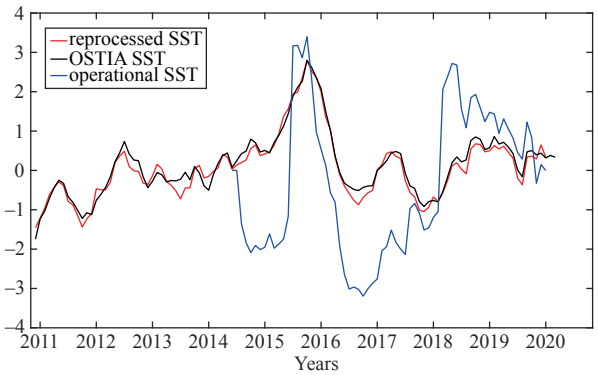


Figure 9. Time series of the Niño-3.4 index from 2011 to 2020.

SST. This could be attributed to the fact that the coefficients, which were influenced by changes in the instrument status, were not updated in a timely manner, and thus the retrieval method employed was not the most current version.

5 CONCLUSIONS

In this study, we analyzed the impacts of the EIA variation on the FY-3/MWRI SST retrieval. Firstly, the influence of the EIA on the channel brightness temperature used for SST retrievals was analyzed based on the microwave radiation transfer model. Then, the variation of SST biases with the EIA considered was analyzed. Finally, an algorithm that incorporated the EIA in the regression was established, and its results were compared with those of the algorithm without the EIA in the regression. The results reveal that the influences of the EIA on the FY-3/MWRI SST retrieval should not be ignored. In contrast to the algorithms that do not consider the EIA in the regression, algorithms integrating the EIA into the regression enhanced the precision of SST retrieval. However, the initial retrieval algorithm for the FY-3B/3C/3D MWRI SST did not consider the impact of the EIA. Consequently, based on the recalibrated FY-3/MWRI Level 1B data, a high-precision long-term SST dataset was reprocessed by employing the algorithm that incorporated the EIA in the regression.

The In-situ SST and the OSTIA SST were used to evaluate the reprocessed FY-3/MWRI SST in terms of product accuracy, long-term stability, and application during El Niño and La Niña events. Comparative analyses suggest that the FY-3/MWRI SST exhibited good agreement with both the in-situ SST and the OSTIA SST. The biases of the FY-3 SST with a quality flag of 50 ranged from −0.2°C to 0.2°C, and the RMSEs varied between 0.2°C and 0.9°C, both demonstrating overall stability. The spatial distributions indicate that notable discrepancies between the FY-3/MWRI SST and the OSTIA SST were located in the regions of the western boundary current and the Antarctic Circumpolar Current. Through a comparison of the climatic monitoring capabilities of the two datasets, it is discerned that the temporal evolution of the Niño-3.4 SST anomalies were

nearly identical to the FY-3 SST and the OSTIA SST, with only slight differences.

There are still some limitations in this study. The in-situ SST was time-averaged at a specific point, whereas the MWRI SST was instantaneous measurements averaged over a large spatial extent (Donlon et al. [43]; Huang et al. [28]), and the measurements were carried out at diverse depths (Okuro et al. [44]), introducing potential errors. Moreover, during the validation by using the OSTIA SST, the impacts of the SST at different depths and the varying time of satellite overpasses were not considered. Therefore, corrections for depths and diurnal variations should be considered in future research to enhance the accuracy of SST validation.

REFERENCES

[1] QIAN Z L, MA J H, YIN Z C. Impacts of the SSTs over equatorial central-eastern Pacific and southeastern Indian Ocean on the cold and rainy/snowy/icy weather in southern China [J]. Journal of Meteorological Research, 2023, 37(2): 248–261, https://doi.org//10.1007/s13351-023-2128-4

[2] CHEN Y, YAN H M, TAO Y, et al. The relationship between Indian Ocean SST and tropical cyclone genesis frequency over North Indian Ocean in May [J]. Journal of Tropical Meteorology, 2023, 29(3): 359–369, https://doi.org/10.3724/j.1006-8775.2023.027

[3] GUO R Y, PAN W J, KE M L, et al. Diversity on the interannual variations of spring monthly precipitation in southern China and the associated tropical sea surface temperature anomalies [J]. Journal of Tropical Meteorology, 2023, 29(3): 337–346, https://doi.org/10.3724/j.1006-8775.2023.025

[4] PISANO A, MARULLO S, ARTALE V, et al. New evidence of Mediterranean climate change and variability from sea surface temperature observations [J]. Remote Sensing 2020, 12(1): 132, https://doi.org/10.3390/rs12010132

[5] LIU Q Q, LI C H, GU D J, et al. Impacts of sea surface temperature on the interannual variability of winter haze days in Guangdong Province [J]. Journal of Tropical Meteorology, 2023, 29(2): 168–178, https://doi.org/10.46267/j.1006-8775.2023.013

[6] DONG N, XU X D, CAI W Y, et al. The response of anomalous vertically integrated moisture flux patterns related to drought and flood in southern China to sea surface temperature anomaly [J]. Journal of Tropical Meteorology, 2023, 29(2): 179–190, https://doi.org/10.46267/j.1006-8775.2023.014

[7] BI M Y, LI T. Sensitivity of TC size to sea surface temperature in the outer region [J]. Journal of Meteorological Research, 2023, 37(6): 829–840, https://doi.org/10.1007/s13351-023-2185-8

[8] BULGIN C E, MERCHANT C J, FERREIRA D. Tendencies, variability and persistence of sea surface temperature anomalies [R]. Scientific Reports, 2020, 10: 7986, https://doi.org/10.1038/s41598-020-64785-9

[9] KENNEDY J J. A review of uncertainty in in situ measurements and data sets of sea surface temperature [J]. Review of Geophysics, 2014, 52(1): 1–32, https://doi.org/10.1002/2013RG000434

[10] BANZON V, SMITH T M, CHIN T M, et al. A long-term record of blended satellite and in situ sea-surface temperature for climate monitoring, modeling and environmental studies [J]. Earth System Science Data, 2016, 8(1): 165–176, https://doi.org/10.5194/essd-8-165-2016

[11] PASTOR F, VALIENTE J A, KHODAYAR S. A warming Mediterranean: 38 years of increasing sea surface temperature [J]. Remote Sensing, 2020, 12(17): 2687, https://doi.org/10.3390/rs12172687

[12] GENTEMANN C L, WENTZ F J, MEARS C A, et al. In situ validation of Tropical Rainfall Measuring Mission microwave sea surface temperatures [J]. Journal of Geophysical Research: Oceans, 2004, 109(C4): C04021, https://doi.org/10.1029/2003JC002092

[13] ZHANG M, XU N, CHEN L. Fusion SST from infrared and microwave measurement of FY-3D meteorological satellite [J]. Journal of Tropical Meteorology, 2024, 30(1): 89–96, https://doi.org/10.3724/j.1006-8775.2024.009

[14] RICCIARDULLI L, WENTZ F J. Uncertainties in sea surface temperature retrievals from space: Comparison of microwave and infrared observations from TRMM [J]. Journal of Geophysical Research: Oceans, 2004, 109(C12): C12013, https://doi.org/10.1029/2003JC002247.

[15] WENTZ F J, GENTEMANN C, SMITH D, et al. Satellite measurements of sea surface temperature through clouds [J]. Science, 2000, 288(5467): 847–850, https://doi.org/10.1126/science.288.5467.847

[16] WENTZ K, MANASTER A. The microwave climate data center repository [R]. Santa Rosa: Remote Sensing Systems, 2022, https://doi.org/10.56236/RSS-bh

[17] ZHANG P, LU Q F, HU X Q, et al. Latest progress of the Chinese meteorological satellite program and core data processing technologies [J]. Advances in Atmospheric Sciences, 2019, 36(9): 1027–1045, https://doi.org/10.1007/s00376-019-8215-x

[18] XIA X, HE W Y, WU S L, et al. A thorough evaluation of the passive microwave radiometer measurements onboard three Fengyun-3 satellites [J]. Journal of Meteorological Research, 2023, 37: 573–588, https://doi.org/10.1007/s13351-023-2198-3

[19] YANG H, LI X Q, YOU R, et al. Environmental data records from FengYun-3B microwave radiation imager [J]. Advances in Meteorological Science and Technology, 2013, 37(4): 136–143, in Chinese with English abstract

[20] HE W Y, CHEN H, XIA X, et al. Evaluation of the long-term performance of microwave radiation imager onboard Chinese Fengyun satellites [J]. Advances in Atmospheric Sciences, 2023, 40(7): 1257–1268, https://doi.org/10.1007/s00376-023-2199-2

[21] WENTZ F J, MEISSNER T. Supplement 1 Algorithm Theoretical Basis Document for AMSR-E Ocean Algorithms [R]. Santa Rosa: NASA, 2007.

[22] ZHANG M, WANG S J, QIN D Y, et al. The inversion and quality validation of FY-3C MWRI sea surface temperature [J]. Journal of Remote Sensing, 2018, 22(5): 713–722, https://doi.org/10.11834/jrs.20187217, in Chinese with English abstract

[23] ZHANG M, SUN F L, DOU F L, et al. Improving the FY-3D MWRI sea surface temperature based on simulated 6.9 GHz brightness temperature [J]. Meteorological Science and Technology, 2022, 50(2): 189–193, in Chinese with English abstract

[24] YAO P, LU H, ZHAO T, et al. A global daily soil moisture dataset derived from Chinese FengYun Microwave Radiation Imager (MWRI) (2010–2019) [J]. Scientific Data, 2023, 10(1): 133, https://doi.org/10.1038/s41597-023-02007-3

[25] XU F, IGNATOV A. In situ SST Quality Monitor (*i*Quam) [J]. Journal of Atmospheric and Oceanic Technology, 2014, 31(1): 164–180, https://doi.org/10.1175/JTECH-D-13-00121.1

[26] WANG S J, CUI P, ZHANG P, et al. FY-3C/VIRR sea surface temperature products and quality validation [J]. Journal of Applied Meteorology, 2020, 31(6): 729–739, in Chinese with English abstract

[27] ZHAO Y L, LIU P, ZHOU W. Inter-comparison of SST products from *i*Quam, AMSR2/GCOM-W1, and MWRI/FY-3D [J]. Remote Sensing, 2024, 16: 2034, https://doi.org/10.3390/ rs16112034

[28] HUANG B, YIN X, CARTON J A, et al. Understanding differences in sea surface temperature intercomparisons [J]. Journal of Atmospheric and Oceanic Technology, 2023, 40 (4): 455–473, https://doi.org/10.1175/JTECH-D-22-0081.1

[29] ZHANG H, IGNATOV A, HINSHAW D. Evaluation of the in situ sea surface temperature quality control in the NOAA in situ SST Quality Monitor (*i*Quam) system [J]. Journal of Atmospheric and Oceanic Technology, 2021, 38(7): 1249–1263, https://doi.org/10.1175/JTECH-D-20-0203.1

[30] PETRENKO B, IGNATOV A, PRYAMITSYN V, et al. Towards improved quality control of in situ sea surface temperatures from drifting and moored buoys in the NOAA *i*Quam System [J]. Applied Sciences, 2023, 13(18): 10205, https://doi.org/10.3390/app131810205

[31] GOOD S E, FIEDLER E, MAO C, et al. The current configuration of the OSTIA system for operational production of foundation sea surface temperature and ice concentration analyses [J]. Remote Sensing, 2020, 12(4): 720, https://doi.org/10.3390/rs12040720

[32] MERCHANT C. Quick start guide to sea SST CCI products [R]. Oxford: European Space Agency, 2013.

[33] YANG C, LEONELLI F E, MARULLO S, et al. Sea surface temperature intercomparison in the framework of the Copernicus Climate Change Service (C3S) [J]. Journal of Climate, 2021, 34(13): 5257–5283, https://doi.org/10.1175/JCLI-D-20-0793.1

[34] MEISSNER T, WENTZ F J. The emissivity of the ocean surface between 6–90 GHz over a large range of wind speeds and Earth incidence angles [J]. IEEE Transactions on Geoscience and Remote Sensing, 2012, 50(8): 3004–3026, https://doi.org/10.1109/TGRS.2011.2179662

[35] WENG F Z. A multi-layer discrete-ordinate method for vector radiative transfer in a vertically-inhomogeneous, emitting and scatting atmosphere-I Theory [J]. Journal of Quantitative Spectroscopy and Radiative Transfer, 1992, 47 (1): 19–33, https://doi.org/10.1016/0022-4073(92)90076-G

[36] GENTEMANN C L, MEISSNER T, WENTZ F J. Accuracy of satellite sea surface temperatures at 7 and 11 GHz [J]. IEEE Transactions on Geoscience and Remote Sensing, 2010, 48(3): 1009–1018, https://doi.org/10.1109/TGRS.2009.2030322

[37] LI Z C, JIANG G M. Sea surface temperature retrieval from the FY-3D MWRI measurements [J]. IEEE Transactions on Geoscience and Remote Sensing, 2024, 62: 4201010, https://doi.org/10.1109/TGRS.2023.3346819

[38] GENTEMANN C L, WENTZ F J, BREWER M, et al. Passive microwave remote sensing of the ocean: An overview [C]// Proceedings "Oceans From Space" Venice 2010. Barale: JRC Scientific and Technical Reports, 2010: 266.

[39] LIU Y Y, WANG S J, LIU J, et al. Evaluation of FY-3/VIRR sea surface temperature data for climate applications [J]. Journal of Meteorological Research, 2021, 35(6): 952–963, https://doi.org/10.1007/s13351-021-1055-5

[40] GENTEMANN C L, DONLON C J, STUART-MENTETH A, et al. Diurnal signals in satellite sea surface temperature measurements [J]. Geophysical Research Letters, 2003, 30 (3): 1140, https://doi.org/10.1029/2002GL016291

[41] TRENBERTH K. The climate data guide: Niño SST indices (Niño 1+2, 3, 3.4, 4; ONI and TNI) [Z]. Boulder: NCAR, [Available at: https://climatedataguide.ucar.edu/climate-data/nino-sst-indices-nino-12-3-34-4-oni-and-tni, accessed on 2024–08–09].

[42] REYNOLDS R W, SMITH T M, LIU C, et al. Daily high-resolution-blended analyses for sea surface temperature [J]. Journal of Climate, 2007, 20(22): 5473–5496, https://doi.org/10.1175/2007JCLI1824.1

[43] DONLON C J, MINNETT P, GENTEMANN C L, et al. Towards improved validation of satellite sea surface skin temperature measurements for climate research [J]. Journal of Climate, 2002, 15(4): 353–369, https://doi.org/10.1175/1520-0442(2002)015<0353:TIVOSS>2.0.CO;2

[44] OKURO A, KUBOTA M, TOMITA H, et al. Intercomparison of various global sea surface temperature products [J]. International Journal of Remote Sensing, 2014, 35(14): 5394–5410, https://doi.org/10.1080/01431161.2014.926415

[45] ZHANG M, WANG S J, SU D D, et al. Fengyun-3 satellite microwave radiation imager sea surface temperature orbit reprocessed dataset V1 version [DS]. 2024/7/15, http://www.richceos.cn/record/cn/detail.html?doi=10.12185/NSMC.REPROC.RPD.SST.FY3.MWRI.L2.GBAL.ORBIT.NUL.51*85KM.HDF.2024.31.V1

[46] ZHANG M, WANG S J, SU D D, et al. Fengyun-3 satellite microwave radiation imager sea surface temperature daily reprocessed dataset V1 version [DS]. 2024/7/15, http://www.richceos.cn/record/cn/detail.html?doi=10.12185/NSMC.REPROC.RPD.SST.FY3.MWRI.L2.GBAL.POAD.GLL.025KM.HDF.2024.32.V1

[47] ZHANG M, WANG S J, SU D D, et al. Fengyun-3 satellite microwave radiation imager sea surface temperature monthly reprocessed dataset V1 version [DS]. 2024/7/15, http://www.richceos.cn/record/cn/detail.html?doi=10.12185/NSMC.REPROC.RPD.SST.FY3.MWRI.L3.GBAL.POAM.GLL.025KM.HDF.2024.33.V1

Citation: ZHANG Miao, CHEN Lin, XU Na, et al. Influences of Earth Incidence Angle on FY-3/MWRI SST Retrieval and Evaluation of Reprocessed SST [J]. Journal of Tropical Meteorology, 2024, 30(3): 230–240, https://doi.org/10.3724/j.1006-8775.2024.021